3-17-2010

Crossed-Beams and Theoretical Studies of Hyperthermal Reactions of $O(^3P)$ with HCl†

Jianming Zhang
Montana State University-Bozeman

Amy L. Brunsvold
Montana State University-Bozeman

Hari P. Upadhyaya
Bhabha Atomic Research Centre

Timothy K. Minton
Montana State University-Bozeman, tminton@montana.edu

Jon P. Camden
Northwestern University

See next page for additional authors

Publication Info

The Journal of Physical Chemistry A, Volume 114, Issue 14, 2010, pages 4905-4916.

Crossed-Beams and Theoretical Studies of Hyperthermal Reactions of O(^{3}P) with HCl†

Jianming Zhang, Amy L. Brunsvold, Hari P. Upadhyaya, and Timothy K. Minton*

Department of Chemistry and Biochemistry, Montana State University, Bozeman, Montana 59717

Jon P. Camden

Department of Chemistry, University of Tennessee, Knoxville, Tennessee 37996-1600

Sophya Garashchuk

Department of Chemistry & Biochemistry, University of South Carolina, Columbia, South Carolina 29208

George C. Schatz*

Department of Chemistry, Northwestern University, Evanston, Illinois 60208-3113

Received: February 3, 2010; Revised Manuscript Received: March 6, 2010

The reaction of O(^{3}P) with HCl at hyperthermal collision energies (45−116 kcal mol^{-1}) has been investigated with crossed-molecular beams experiments and direct dynamics quasi-classical trajectory calculations. The reaction may proceed by two primary pathways, (1) H-atom abstraction to produce OH and Cl and (2) H-atom elimination to produce H and ClO. The H-atom abstraction reaction follows a stripping mechanism, in which the reagent O atom approaches the HCl molecule at large impact parameters and the OH product is scattered in the forward direction, defined as the initial direction of the reagent O atoms. The H-atom elimination reaction is highly endoergic and requires low-impact-parameter collisions. The excitation function for ClO increases from a threshold near 45 kcal mol^{-1} to a maximum around 115 kcal mol^{-1} and then begins to decrease when the ClO product can be formed with sufficient internal energy to undergo secondary dissociation. At collision energies slightly above threshold for H-atom elimination, the ClO product scatters primarily in the backward direction, but as the collision energy increases, the fraction of these products that scatter in the forward and sideways directions increases. The dependence of the angular distribution of ClO on collision energy is a result of the differences in collision geometry. Collisions where the H atom on HCl is oriented away from the incoming reagent O atom lead to backward-scattered ClO and those where the H atom is oriented toward the incoming O atom lead to forward-scattered ClO. The latter trajectories do not follow the minimum energy path and involve larger translational energy release. Therefore, they become dominant at higher collision energies because they lead to lower internal energies and more stable ClO products. The H-atom abstraction and elimination reactions have comparable cross sections for hyperthermal O(^{3}P) + HCl collisions.

I. Introduction

The reaction of O(^{3}P) with HCl may follow two primary reaction pathways,

$$O(^3P) + HC1 \rightarrow OH + C1 \qquad \Delta H^\circ_{f,0} = 0.5 \text{ kcal mol}^{-1} \tag{1}$$

$$\rightarrow C1O + H \qquad \Delta H^\circ_{f,0} = 38.9 \text{ kcal mol}^{-1} \tag{2}$$

Reaction 1 is almost thermo-neutral, and the barrier appears to be 10.6 kcal mol^{-1}.[1] It has been studied extensively, both experimentally and theoretically, because of its important role in the chemistry of the stratospheric ozone layer[2,3] and its fundamental interest as a benchmark for hydrogen atom transfer reactions in heavy + light-heavy (H + LH) systems.[4,5] Experimental studies have mainly focused on thermal and high temperature rate studies and reagent state resolved rate measurements. Reviews of the work can be found in several articles.[6−9] State-to-state integral cross sections for rovibronically excited HCl have also been measured.[5,10] On the theoretical side, several potential energy surfaces (PESs) have been constructed for this reaction. The first was a London−Eyring−Polanyi−Sato (LEPS) surface, which does not account for the fact that there are two potentials (^{3}A′ and ^{3}A″) that correlate the ground states of the reagents and products.[11−14] The LEPS surface has a linear configuration at the saddle point. On the basis of MP2/6-31G(d,p) calculations, Koizumi, Schatz, and Gordon[6,15] developed the first ab initio potential energy surface for ^{3}A″, denoted as the KSG surface, which has a bent saddle point geometry with an O−H−Cl angle of 133.4° and a reaction barrier of 8.5 kcal mol^{-1}. The ^{3}A″ surface is degenerate with the ^{3}A′ surface at a linear O−H−Cl saddle point, which is 1.9 kcal mol^{-1} higher than that of the bent saddle point. Comparison of experiments and calculations based on this surface has shown that the reaction barrier is too low.[16−18] Ramachandran et al. have

† Part of the special section "30th Free Radical Symposium".

* Authors to whom correspondence should be addressed. Electronic mail: T.K.M., tminton@montana.edu; G.C.S., schatz@chem.northwestern.edu.

10.1021/jp101023y
Published on Web 03/17/2010

conducted a series of calculations on a new $^3A''$ PES based on a multireference configuration interaction level of theory with the Davidson correction (MRCI-Q) using the Dunning cc-pVTZ one-electron basis sets.[7,8,19] The reaction barrier on this surface is 9.78 kcal mol^{-1} and has an O−H−Cl angle of 131.4°. Quantum mechanical calculations of the thermal rate coefficients on this surface have shown that the reaction barrier may be too low and too narrow.[20−22] The first global PES for $^3A'$ and the newest and most accurate global PES to date for $^3A''$ were calculated at the MRCI-Q/CBS level of theory by Ramachandran and Peterson,[1] denoted as RP surfaces. The reaction barrier on the $^3A''$ surface is 10.60 kcal mol^{-1} with an O−H−Cl angle of 135.9°. The collinear barrier of 13.77 kcal mol^{-1} on the $^3A''$ surface is located further into the exit channel than the bent saddle point and is degenerate with the saddle point on the $^3A'$ surface. Quantum calculations of the rate constant on this surface have shown that the $^3A'$ surface has no significant contribution to the total thermal rate constant at lower temperatures but becomes more important with increasing temperature.[23] Xie et al. have performed quantum and quasi-classical calculations on the RP surfaces with collision energies from threshold to ∼130 kcal mol^{-1}.[24] The results are only qualitative above ∼40 kcal mol^{-1} since this is beyond the reported valid range of the RP surfaces. They discovered that the energy is partitioned into translation and rotation, which is consistent with a late barrier to reaction. Angular distributions of OH at high collision energies are forward peaked in the center-of-mass (c.m.) reference frame, consistent with a stripping mechanism.

The rich literature of both experimental and theoretical work made reaction 1, the H-atom abstraction channel, a test bed for various dynamics studies. However, little work has been done on reaction 2, the H-atom elimination channel. Reaction 2 is highly endoergic, which makes it difficult to study this reaction experimentally. Figure SI-1 (Supporting Information) shows a schematic energy diagram for different pathways when O(^{3}P) atoms react with HCl. The H-atom abstraction channel has the lower barrier, but at collision energies greater than ∼45 kcal mol^{-1}, the H-atom elimination channel becomes accessible. At collision energies greater than ∼102 kcal mol^{-1}, fragmentation into three atoms becomes energetically allowed. Therefore, at hyperthermal collision energies, both reactions 1 and 2, as well as secondary dissociation of ClO from reaction 2, may be open.

Hyperthermal reactions of O(^{3}P) with HCl may play a role in the interactions of rocket exhaust streams with the ambient atmosphere at low Earth orbit (LEO).[25] At LEO altitudes of 200−700 km, O(^{3}P) is the dominant species in the atmosphere,[26] while HCl is an important species in rocket exhaust streams.[25] The relative velocities of O(^{3}P) and HCl are in the vicinity of 8 km s^{-1},[26,27] which results in collision energies of ∼85 kcal mol^{-1} in the c.m. reference frame. Although both primary reaction channels are open at this collision energy, the branching ratio and detailed dynamics of the two channels at hyperthermal collision energies have remained unknown.

The H-atom elimination channel is also of fundamental interest, as it is unique for hyperthermal reactions of the type heavy + heavy-light (H + HL).[28−30] The first reported study on the H-atom elimination channel of O(^{3}P) + HCl was reported by Camden and Schatz,[29] who conducted direct dynamics calculations on reactions 1 and 2 at hyperthermal collision energies, in the range, 69.18−161.42 kcal mol^{-1}. The calculated barrier for H-atom elimination is 43.68 and 52.12 kcal mol^{-1}, based on the B3LYP/6-31G(d,p) and CCSD(T)/cc-pVTZ levels of theory, respectively. Results from the MP2/cc-pVTZ level of theory showed that with a collision energy of 115.3 kcal mol^{-1}, ClO is formed mainly from small-impact-parameter collisions and scattered into the backward direction with respect to the initial direction of the reagent O atom in the c.m. reference frame. The calculated excitation function rises from a threshold near 45 kcal mol^{-1} and has a maximum at ∼115.3 kcal mol^{-1}. The secondary dissociation of ClO becomes increasingly important at higher collision energies, and the cross section for production of intact ClO is diminished. Recently, Camden et al.[31] used an automated interpolating moving least-squares (IMLS) algorithm and constructed a global OHCl ($^3A''$) surface at the UB3LYP/aug-cc-pVTZ level of theory. The fitted surface was combined with the quasi-classical trajectory (QCT) method to study the dynamics of the O(^{3}P) + HCl reaction at hyperthermal collision energies. The more extensive trajectory calculations agreed well with previous direct dynamics results. Besides the above theoretical studies, we have also published a short report of a combined experiment-theory study of the H-atom elimination channel.[30] Two distinct dynamical mechanisms were identified, and the dominant mechanism at high collision energies was found to correspond to motion far from the minimum energy path. This finding is believed to be a general feature of light atom eliminations in hyperthermal reactions with H + HL mass combination. For example, H-atom elimination was also observed in hyperthermal O-atom reactions with H_2O,[32] and the dynamics were found to be analogous.

Here we present a full report of crossed-molecular beams and theoretical studies of hyperthermal reactions of O(^{3}P) with HCl. Experimentally, we investigated the dynamics of H-atom abstraction and elimination with collision energies of 69.1 and 92.2 kcal mol^{-1}. We also measured the relative excitation function of H-atom elimination in the collision energy range of 45−116 kcal mol^{-1}. The dynamics of these two reaction channels and the excitation function of the H-atom elimination channel were also calculated theoretically. These calculations provide detailed insight into aspects of O(^{3}P) + HCl collision dynamics which are inaccessible in the experiment.

II. Details of the Quasiclassical Trajectory Calculations

Application of the direct dynamics quasi-classical trajectory method to the O + HCl system is described in a previous publication;[29] therefore, we only provide relevant details here. The calculations were performed with the reagent HCl (or DCl) molecules in their lowest rotational state ($j = 0$), which approximates the experimental conditions where HCl is cooled to low rotational states in the supersonic expansion (see section III). Batches of 900 quasiclassical trajectory calculations were run at a variety of collision energies (E_{coll}) between 46 and 161 kcal mol^{-1} to calculate reaction cross sections for the ClO + H (σ_{OCl}) and O + H + Cl (fragmentation, σ_{frag}) product channels. The reactive trajectories were classified according to the angle γ, which is the angle between the O-atom velocity vector and the H−Cl bond axis when the reagents are well separated.[30] We note that, at the large relative velocities and low rotational states probed here, γ remains approximately constant during the interaction time of a collision. All calculations were performed on the ground triplet state surface ($^3A''$); however, we have discussed previously the possible contribution of the first excited triplet state ($^3A'$).[29] Trajectories were integrated by a standard fifth-order predictor, sixth-order corrector integration algorithm.[33,34] At each point along the trajectory, the energy and gradient were obtained from a B3LYP/6-31G(d,p) calculation in Q-Chem. MP2/cc-pVTZ calculations were also run and agree qualitatively with the B3LYP results; however, the better description of the experimental results and lower computational

cost using B3LYP led us to focus our efforts at this level of theory. (Note that the theoretical results reported here for the reaction, O(^{3}P) + HCl → OH + Cl and O(^{3}P) + DCl → ClO + D, were obtained from QCT calculations on the IMLS surface of Camden, Dawes, and Thompson,[31] which is a B3LYP-fitted surface that gives quantitative agreement with the direct dynamics calculations.) The initial conditions were sampled randomly over initial orientations and impact parameter. A single intramolecular trajectory starting from the equilibrium HCl geometry was run with a kinetic energy corresponding to the zero-point vibrational energy. The HCl vibrational phase for each reactive trajectory was then sampled randomly from the initial intramolecular trajectory. The maximum impact parameter (b_{max}) was 3.0 au. In each batch of trajectories, our choice of b_{max} was justified by examination of the opacity function, which indicates that the O + HCl → ClO + H reaction occurs preferentially at small impact parameters, greatly reducing the computational cost required to obtain good statistics. The integration time step was held constant at 10.0 au for all trajectories. Energy conservation was required to be better than 3 kcal mol^{-1} in total energy, and spin contamination was checked at each time step during trajectory propagation. Less than 0.1% of the trajectories violated energy conservation, and these violations were attributed to problems in convergence of the self-consistent field (SCF) calculation (i.e., the SCF failed to converge or converged to the wrong electronic state during trajectory propagation) and not the integration time step. For the higher energies, larger values of spin contamination were observed for trajectories that led to fragmentation, which is expected as several bonds are broken. We retained these trajectories, however, because their neglect would have led to inaccurate fragmentation cross sections. Integration was terminated when the distance between any two atoms exceeded 10 au. We did not discard product trajectories with an internal energy below the harmonic zero point, as this can lead to an underestimation of the cross section.[35−37] When fragmentation occurs, the light H atom can often move beyond the 10 au limit before ClO can separate. In these cases we calculated the internal energy of the ClO product, and if it exceeded the threshold for fragmentation into H + Cl + O, we assigned that trajectory to fragmentation.

QCT calculations on the KSG potential energy surface have also been conducted for the reactions of O(^{3}P) with HCl and DCl, to illustrate the isotope effect. For O + HCl, the results are qualitatively in agreement with those of B3LYP calculations. The results of the QCT calculations on the KSG surface are shown in Supporting Information and are referred to at appropriate points in the manuscript below.

III. Experimental Methods

The experiments were performed with the use of a crossed molecular beams apparatus equipped with a fast-atom beam source.[38−40] Details about the experimental apparatus can be found in an earlier paper.[41] In general, a pulsed, hyperthermal beam of oxygen atoms was crossed at right angles with a pulsed, supersonic beam of HCl (or DCl) gas (Matheson, 99.995%). Both beams were operated at a repetition rate of 2 Hz. Products that scattered from the interaction region were detected with a rotatable mass spectrometer detector that measured number density distributions as a function of arrival time, $N(t)$, which are commonly referred to as time-of-flight (TOF) distributions. TOF distributions collected at different detector angles were integrated to give laboratory angular distributions $N(\Theta)$. Θ is the angle of the scattered product with respect to the O-atom beam. These data were collected in the laboratory reference frame, and a forward-convolution method was employed to derive c.m. quantities from the laboratory TOF and angular distributions.[41−44]

A supersonic expansion of HCl was created with a piezoelectric pulsed valve, with a nozzle diameter of 1.0 mm, from a stagnation pressure of 15 psig. The HCl beam passed through a 5-mm-diameter skimmer and a 3-mm-diameter aperture before crossing the O-atom beam. The distance between the nozzle and skimmer was 9.2 cm, and the distance from the skimmer to the 3-mm-diameter aperture was 2.8 cm. From the aperture, the beam traveled 1.5 cm to the crossing point of the two beams. The HCl beam velocity was estimated to be ~700 m s^{-1}.[45] The velocity of the HCl beam was an order of magnitude lower than that of the O-atom beam, and the velocity width of the HCl beam was not considered in the experiment.

The hyperthermal oxygen beam was produced with a laser-breakdown source based on the original design of Caledonia et al.[46] The beam pulse passed through a 7-mm-diameter aperture located 80 cm from the apex of the conical nozzle into a differential pumping region and then passed through a 3-mm-diameter skimmer positioned 16 cm from the aperture before reaching the main scattering chamber. To prepare hyperthermal oxygen beams with relatively narrow and variable velocity distributions, a narrower range of velocities was selected from the overall beam pulse with the use of a synchronized chopper wheel, rotating at 300 Hz and placed about 97 cm from the apex of the conical nozzle. The hyperthermal beam reached the interaction region 99 cm from the nozzle apex. The velocity distributions in the O-atom beam pulses were determined by the time-of-flight method. Several hyperthermal O beams were used in the experiments. The average translational energies of the O beams were in the range, 62−167 kcal mol^{-1}, and the mole fraction of atomic oxygen in the beams was approximately 80%. The average collision energy in the c.m. reference frame was derived from the average velocity of the O-atom beam and the nominal velocity of the HCl beam using the equation, $E_{coll} = (1/2)\mu v_{rel}^2$, where μ is the reduced mass and v_{rel} is the relative velocity of the O atom and the HCl molecule. Figure SI-2 (Supporting Information) shows the collision energy distributions of oxygen atoms for 8 representative beams. The average collision energies in this experiment varied from 45 to 116 kcal mol^{-1}, and the width of the collision energy distributions (fwhm) ranged from 10 to 20 kcal mol^{-1}. To have better dynamical resolution for reactively scattered ClO, DCl was also used as a reagent. DCl gas was obtained from Cambridge Isotope Laboratories: 99% DCl with the remainder being HCl. The dynamical differences in the scattered products from the reactions of O(^{3}P) with HCl and DCl, with E_{coll} = 92.2 kcal mol^{-1}, are illustrated in the Newton diagrams in Figure SI-3 (Supporting Information).

Inelastically scattered O and O_2 were collected at m/z = 16 and 32, with integrated count rates in the ranges 2.0 × 10^4 to 3.5 × 10^5 and 4.0 × 10^4 to 6.5 × 10^5 counts s^{-1}, respectively. TOF distributions collected at m/z = 16 were corrected by subtracting 11% of the TOF distribution collected at m/z = 32 to account for the signal at m/z = 16 that comes from dissociative ionization of O_2. Reactively scattered OH and ClO were collected at m/z = 17 and 51, with integrated count rates in the ranges 700−2500 and 7.0 × 10^3 to 2.5 × 10^5 counts s^{-1}, respectively. TOF distributions for ^{16}OD (m/z = 18) are not reported here, because the signal was weak and the background at m/z = 18 in the detector was relatively high, and because there was overlapping signal from inelastic scattering of ^{18}O

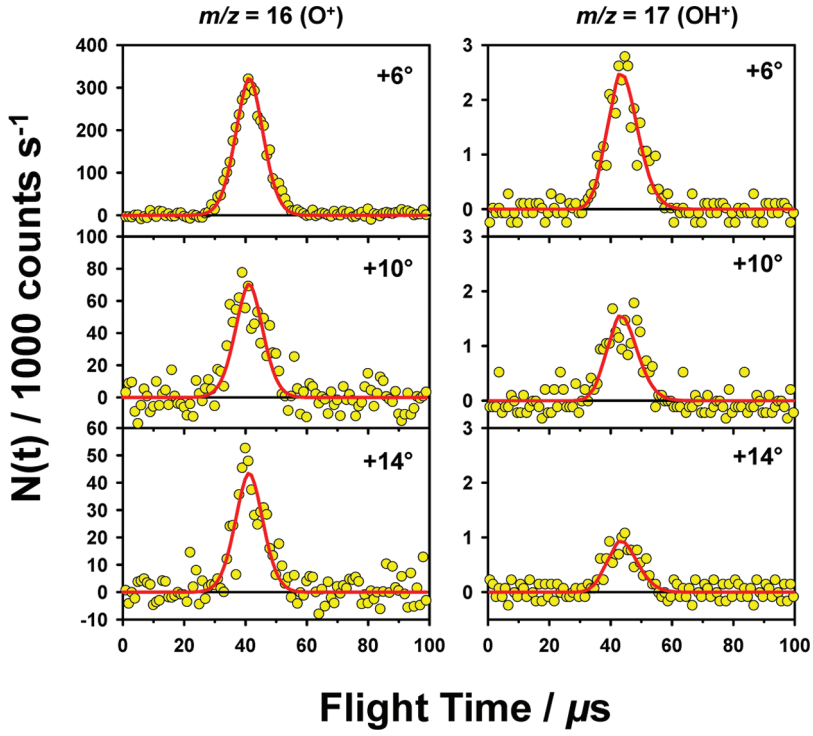

Figure 1. Representative time-of-flight distributions of inelastically scattered O and reactively scattered OH following collision of O(^{3}P) with HCl at $\langle E_{coll} \rangle$ = 92.2 kcal mol^{-1}. The circles are the experimental data. The red curves are the forward-convolution fits to the data, derived from the corresponding c.m. angular and translational energy distributions shown in the bottom panels of Figure 3.

that was in the reagent beam at 0.2% natural abundance. At each laboratory angle, different products were signal averaged with different numbers of beam pulses because of the different signal levels. TOF distributions were collected for 3000 beam pulses for OH, 1000 beam pulses for ClO, and 200 beam pulses for O and O_2. The laboratory angle was adjusted in 2° increments until the entire angular range was covered. Then the increment direction was reversed and the cycle was repeated until a total of four TOF distributions had been collected for each product at each detector angle. The sum of the four TOF distributions gives one TOF distribution at each detector angle, which accounts for long-term drifts in the experimental parameters. Laboratory angular distributions were obtained by integrating the TOF distributions collected at the various detector angles. From the forward-convolution method,[41] c.m. angular and translational energy distributions were obtained by fitting the laboratory TOF and angular distributions.

The forward-convolution method also yields relative integrated reaction cross sections. These were used to derive the experimental excitation function for the H-atom elimination reaction (reaction 2). In general, experimental determination of excitation functions by this method is best suited for reactions whose products have small Newton spheres, as the products are scattered at small solid angles and can be detected over a narrow laboratory angular range. For products whose recoil velocities in the c.m. frame are much smaller than the velocity of the c.m. in the laboratory frame, the measurement of the product flux at the c.m. angle in the laboratory frame provides a good approximation of the relative product flux for the whole Newton sphere. We have used such measurements to determine relative excitation functions for the reactions, $O + H_2 \rightarrow OH + H$,[47] $O + CH_4 \rightarrow OCH_3 + H$,[48] and $O + H_2O \rightarrow HO_2 + H$.[32] However, for the reaction, $O + HCl \rightarrow ClO + H$, the c.m. recoil velocities of ClO are relatively large compared to the velocity of the c.m. in the laboratory frame. The ClO product is thus scattered in a relatively large range of solid angles compared to ranges for the products of the reactions studied earlier. Therefore, TOF distributions of ClO were collected over a range of laboratory angles that covered the whole Newton sphere. Fitting the data with the forward-convolution method provided a relative integrated reaction cross section, which is proportional to the flux of the products scattered over the whole Newton sphere. The obtained integrated reaction cross section was normalized to the flux of the incident O-atom beam by taking the flux of inelastically scattered O atoms to be proportional to the flux of O atoms in the beam.[32] The flux of inelastically scattered O atoms was measured at the angle of the c.m. in the laboratory frame. The importance of integrating the scattered flux of ClO over the whole Newton sphere is illustrated in Figure SI-4 (Supporting Information).

IV. Results

Representative TOF distributions for inelastically scattered O and reactively scattered OH at collision energies of 69.1 and 92.2 kcal mol^{-1} are shown in Figure SI-5 (Supporting Information) and Figure 1, respectively. The laboratory angular distributions are shown in Figure 2. The solid curves in the figures are the forward-convolution fits to the TOF distributions and laboratory angular distributions for O and OH, based on the corresponding c.m. angular and translational energy distributions in Figure 3. Both O and OH products are strongly forward scattered with respect to the initial direction of the reagent O atoms. As can be seen in the Newton diagram (Figure SI-3, Supporting Information), the laboratory detection angles are primarily sensitive to O and OH that scatter into the forward hemisphere (0 to ~35° in the c.m. reference frame), so only the corresponding angular range in the c.m. angular distributions that was accessible in the experiment was used in the forward-convolution analysis. The translational energy distributions show that, on average, about 86% and 93% of the available energy is

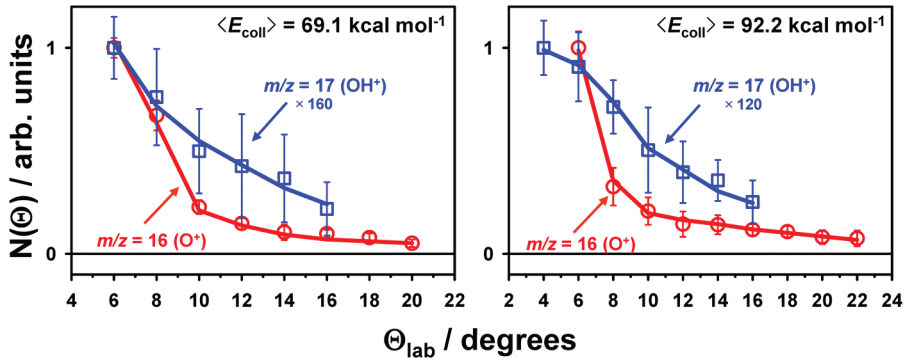

Figure 2. Laboratory angular distributions of inelastically scattered O and reactively scattered OH following collision of O(^{3}P) with HCl at $\langle E_{coll} \rangle$ = 69.1 and 92.2 kcal mol^{-1}. The open circles and squares with error bars are the experimental data, and the solid lines are the forward-convolution fits to the data, derived from the corresponding c.m. angular and translational energy distributions in Figure 3. The error bars are estimated from fitting the experimental TOF distributions with a modified Gaussian function and finding areas of the maximum and minimum acceptable fits by adjusting the Gaussian parameters. The error bars thus represent the maximum and minimum integrals of the TOF distributions based on our best judgment.

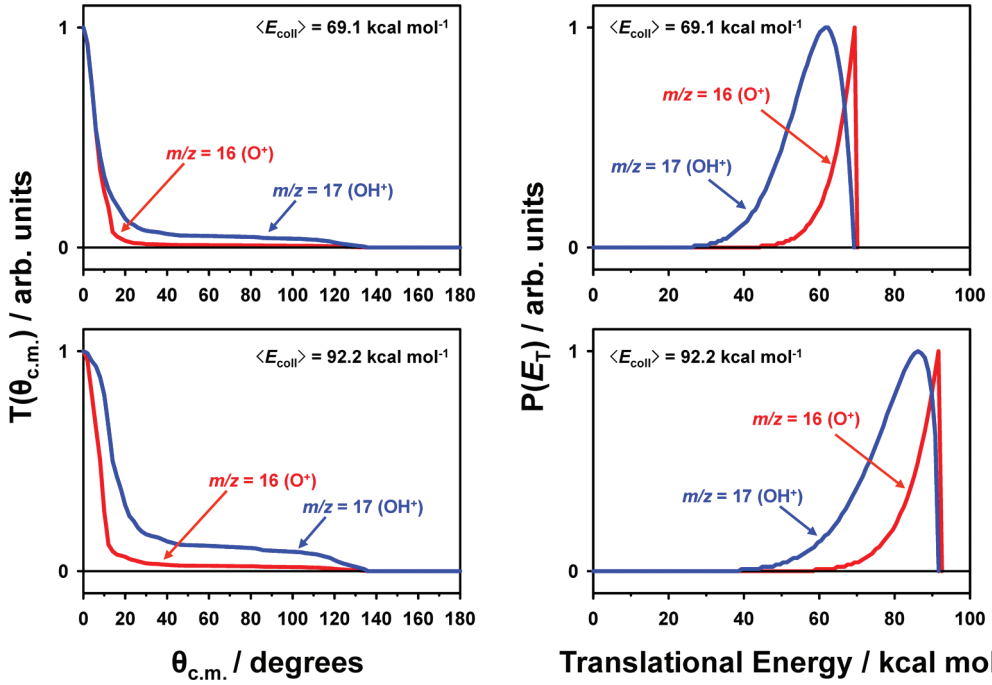

Figure 3. Center-of-mass angular and translational energy distributions for inelastic scattering of O and reactive scattering of OH following collision of O(^{3}P) with HCl at $\langle E_{coll} \rangle$ = 69.1 and 92.2 kcal mol^{-1}, used in the forward-convolution fit of the laboratory TOF and angular distributions for O and OH in Figures 1, 2, and SI-5 (Supporting Information). The distributions were determined by optimizing the c.m. distributions to fit the data.

released in translation in the reactive and inelastic channels, respectively. Figure 4 shows the OH c.m. angular and translational energy distributions calculated from direct dynamics simulations at the B3LYP/6-31G(d,p) level of theory. The theoretical results also show that OH is strongly forward scattered and that, on average, about 72% of the energy goes into translation for the H-atom abstraction reaction. The center-of-mass angular and translational energy distributions for reactive scattering of OH and OD from QCT calculations on the KSG surface for the reactions of O(^{3}P) with HCl and DCl at collision energies of 69.1 and 92.2 kcal mol^{-1} are shown in Figure SI-6 (Supporting Information).

Representative TOF distributions of reactively scattered ClO for the reactions, O + HCl → ClO + H and O + DCl → ClO + D, are shown in Figure SI-7 (Supporting Information) and Figure 5, respectively, for collision energies of 69.1 and 92.2 kcal mol^{-1}. The corresponding laboratory angular distributions are shown in Figure 6. The TOF distributions of ClO near the c.m. angle in the laboratory frame (12°) clearly show bimodal distributions, suggesting forward (shorter flight times) and backward (longer flight times) scattering in the c.m. reference frame. The bimodal nature of the TOF distributions is more obvious in Figure 7, which shows TOF distributions of ClO that were collected for several collision energies at a laboratory detection angle corresponding to the velocity vector of the center of mass. It is apparent that the reaction probability increases from a collision energy of about 45 kcal mol^{-1} and the relative fraction of forward-scattered ClO increases with collision energy. It is also clear that the forward and backward components are more separated for the reaction O + DCl → ClO + D than for the reaction O + HCl → ClO + H. During the forward-convolution fitting of the TOF and laboratory angular distributions, we found that one set of $P(E)$ and $T(\theta)$ distributions would not give good fits to the data, which indicated that there is a dependence of the $P(E)$ distribution on the c.m. scattering angle.[41−44] In general, the forward-scattered ClO

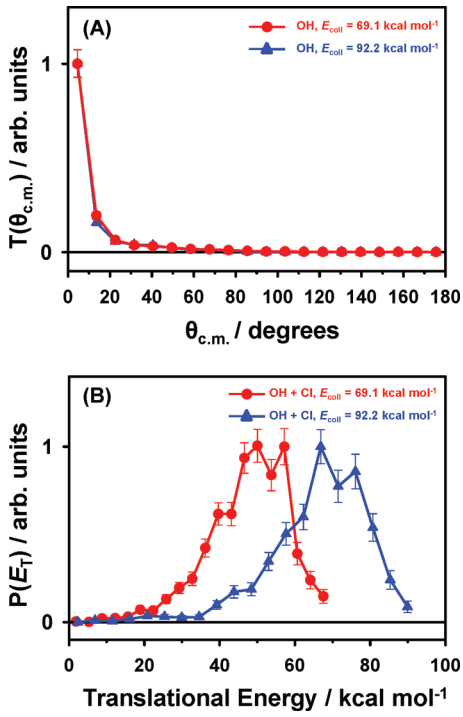

Figure 4. Center-of-mass angular and translational energy distributions for reactive scattering of OH from direct dynamics calculations at the B3LYP/6-31G(d,p) level of theory.

products involve a larger translational energy release than the products scattered in the backward direction. This feature is more apparent at the higher collision energy. To obtain satisfactory fits to the experimental data, two separate sets of $P(E)$ and $T(\theta)$ distributions were used in the forward-convolution fitting procedure, with one for forward scattering and one for backward scattering. As discussed at length previously,[41] the derived c.m. angular and translational energy distributions are not entirely unique because of the limited resolution of the data. Small variations in the c.m. distributions can still result in fits to the data that are within the uncertainties of the data. The error ranges of the derived c.m. distributions may be as high as ±10%. Nevertheless, even accounting for the lack of uniqueness, it was not possible to obtain acceptable fits to all the data with a single set of $P(E)$ and $T(\theta)$ distributions. Two sets of these distributions were sufficient to provide good fits to all the data. The solid curves in Figure SI-7 (Supporting Information) and Figures 5 and 6 are the forward-convolution fits to the data. The c.m. angular and translational energy distributions are shown in Figures 8, 9, SI-8, and SI-9. The fact that experimentally derived c.m. angular distributions in these figures do not have smooth transitions from forward to backward scattering is an artifact of the use of just two sets of $P(E)$ and $T(\theta)$ distributions to account for the coupling between c.m. translational energy and angle. Smoother overall angular distributions could have been obtained by using more sets of $P(E)$ and $T(\theta)$ distributions in the forward-convolution procedure, but the data did not have sufficient resolution to justify the use of more than two sets. The energy released into translation when ClO is scattered forward is larger than that when ClO is scattered backward. At a collision energy of 69.1 kcal mol^{-1}, ClO is mainly backward scattered. As the collision energy increases, the forward-scattering component increases. It appears that two distinct mechanisms are responsible for the two components.

The experimental results are consistent with theoretical calculations, as shown in Figures 8, 9, SI-8, and SI-9. (Results from the calculations on the KSG surface are shown in Figure SI-10 (Supporting Information).) The calculated "total" c.m. angular distributions clearly show that the ClO scattering shifts from more backward to more forward with increasing collision

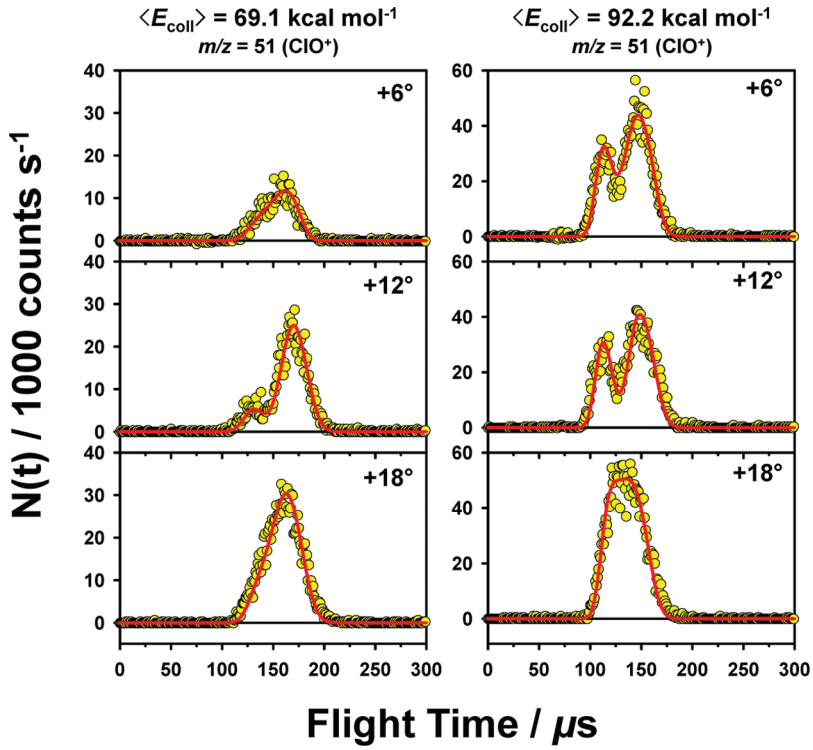

Figure 5. Representative time-of-flight distributions of reactively scattered ClO following reaction of $O(^3P)$ with DCl at $\langle E_{coll} \rangle$ = 69.1 and 92.2 kcal mol^{-1}. The circles are the experimental data. The solid curves are the forward-convolution fits to the data, derived from the corresponding c.m. angular and translational energy distributions in Figures SI-9 (Supporting Information) and 9.

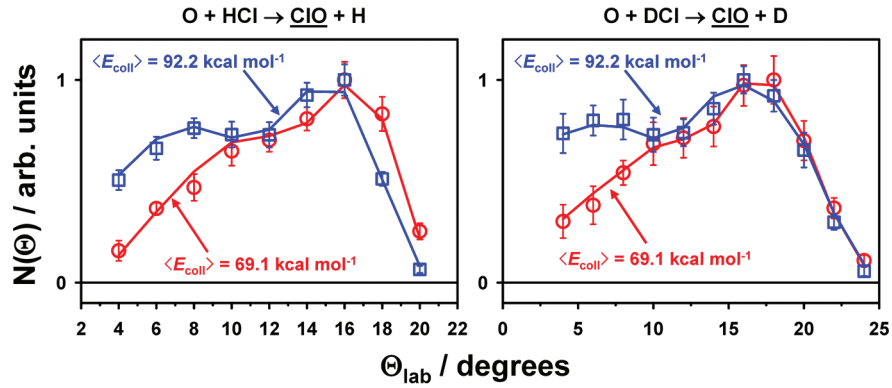

Figure 6. Laboratory angular distributions of reactively scattered ClO following reaction of O(3P) with HCl or DCl at $\langle E_{coll} \rangle = 69.1$ and 92.2 kcal mol^{-1}. The open circles and squares with error bars are the experimental data, and the solid lines are the forward-convolution fits to the data, derived from the corresponding c.m. angular and translational energy distributions in Figures 8, 9, SI-8, and SI-9. The error bars are estimated from fitting the experimental TOF distributions with a modified Gaussian function and finding areas of the maximum and minimum acceptable fits by adjusting the Gaussian parameters. The error bars thus represent the maximum and minimum integrals of the TOF distributions based on our best judgment.

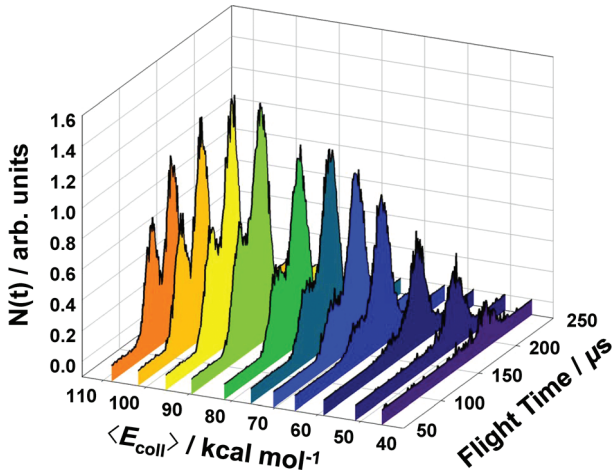

Figure 7. Time-of-flight distributions of reactively scattered ClO following reaction of O(3P) with HCl. The TOF distributions were collected at laboratory c.m. scattering angles and at eleven collision energies. The ClO flux has been normalized to the inelastically scattered O flux.

energies. The calculations also demonstrate that collisions with $\gamma < 90°$ produce forward-scattered ClO with a relatively large release of translational energy, whereas collisions with $\gamma > 90°$ produce backward-scattered ClO with less energy released in translation. Note that trajectories with $\gamma > 90°$ roughly follow the minimum energy path to produce ClO + H, while trajectories with $\gamma < 90°$ deviate significantly from the minimum energy path. The average translational energy as a function of c.m. scattering angle, derived from the experiment and theory, is shown in Figure 10.

Figure 11 shows the c.m. velocity-flux maps derived from the sets of angular and translational energy distributions shown in Figures 8, 9, SI-8, and SI-9. At the lower collision energy, ClO is mainly backward scattered, and the fraction of ClO scattered in the forward direction increases with collision energy.

Experimental and theoretical results for various excitation functions associated with the O + HCl reaction are shown in Figure 12. Because the experimental excitation function for ClO is only relative, it has been normalized to give the best match to the theoretical excitation function so that the shapes of the two curves may be compared. The cross section for ClO formation rises from threshold (~46 kcal mol^{-1}) and becomes comparable in cross section for OH formation at $E_{coll} = 90-120$ kcal mol^{-1}. At higher collision energies, the ClO cross section decreases as a result of secondary dissociation to Cl + O.

The branching ratio between the OH + Cl channel (reaction 1) and the ClO + H channel (reaction 2) has also been determined experimentally. The integrated intensities of OH and ClO from forward-convolution analyses were used to calculate the branching ratio. Differences in total ionization cross sections for OH[49,50] and ClO[51,52] have been considered. The fragmentation pattern for electron impact ionization was assumed be the same for the two diatomic species.[53] The transmission of the quadrupole was assumed to be constant over the range of masses under consideration. The OH/ClO branching ratio was determined to be 1.5 and 0.8 for collision energies of 69.1 and 92.2 kcal mol^{-1}, respectively. The corresponding branching ratios from theory (B3LYP) were 2.4 and 1.2, respectively. The ratio between the experimental and theoretical OH/ClO branching ratios at the two collision energies are quite similar, i.e., 1.5/0.8 ≈ 2.4/1.2.

V. Discussion

A. Inelastic Scattering. As expected for inelastic collisions, O atoms are strongly forward scattered, with respect to the initial direction of the reagent O atoms, in the c.m. reference frame, and HCl molecules are scattered in the backward direction. The c.m. translational energy distribution shows that on average ~94% of the collision energy is partitioned into translation. The observation of little change in direction and energy shows that inelastic scattering tends to occur with large impact parameters. Nevertheless, the slow energy tail in the translational energy distribution indicates that a significant amount of energy can still be transferred into the internal energy of HCl, presumably from lower probability collisions with relatively small impact parameters. Subtracting the translational energy distribution from the collision energy gives the internal energy distribution of HCl, which shows that some collisions can transfer more than ~19 and ~25 kcal mol^{-1} of energy into the internal energy of HCl for collision energies of 69.1 and 92.2 kcal mol^{-1}, respectively. This indicates that some collisions can excite HCl into $v' = 1$ or $v' = 2$ for collision energies of 69.1 and 92.2 kcal mol^{-1}, respectively. Calculations by Xie et al.[24] showed that the cross section for direct collisional excitation of HCl into $v' = 1$ becomes significant at a collision energy of 21.2 kcal mol^{-1} and increases rapidly when the collision energy is greater than 47.5 kcal mol^{-1}. Direct collisional excitation has

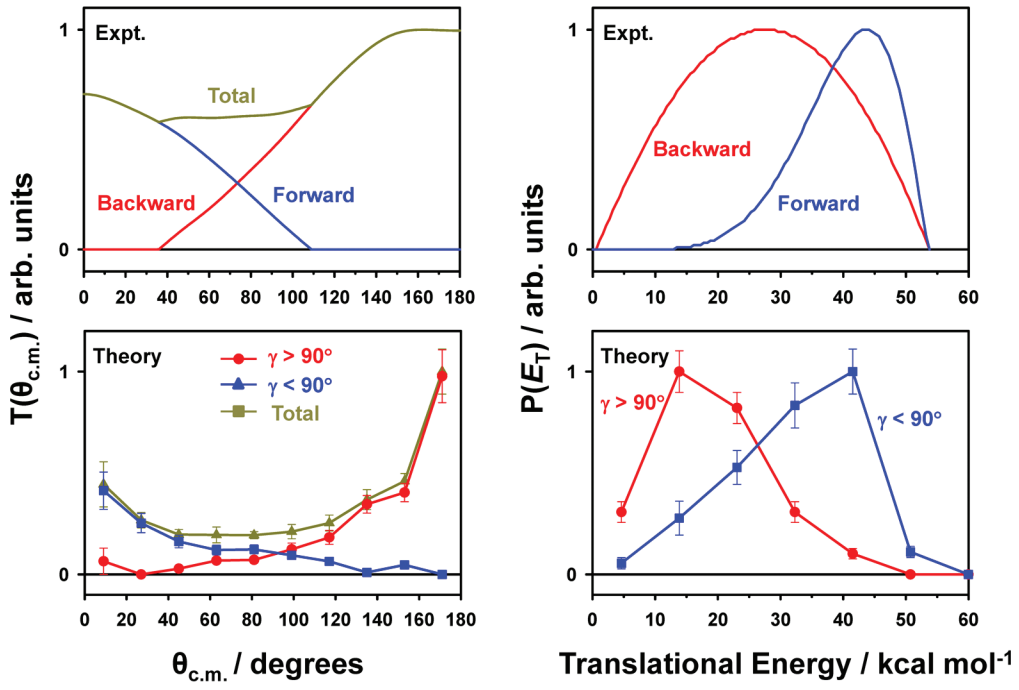

Figure 8. Center-of-mass angular and translational energy distributions for reactive scattering of ClO following reaction of $O(^3P)$ with HCl at $\langle E_{coll} \rangle = 92.2$ kcal mol^{-1}, derived from experiment (top panels) and from direct dynamics calculations at the B3LYP/6-31G(d,p) level of theory (bottom panels).

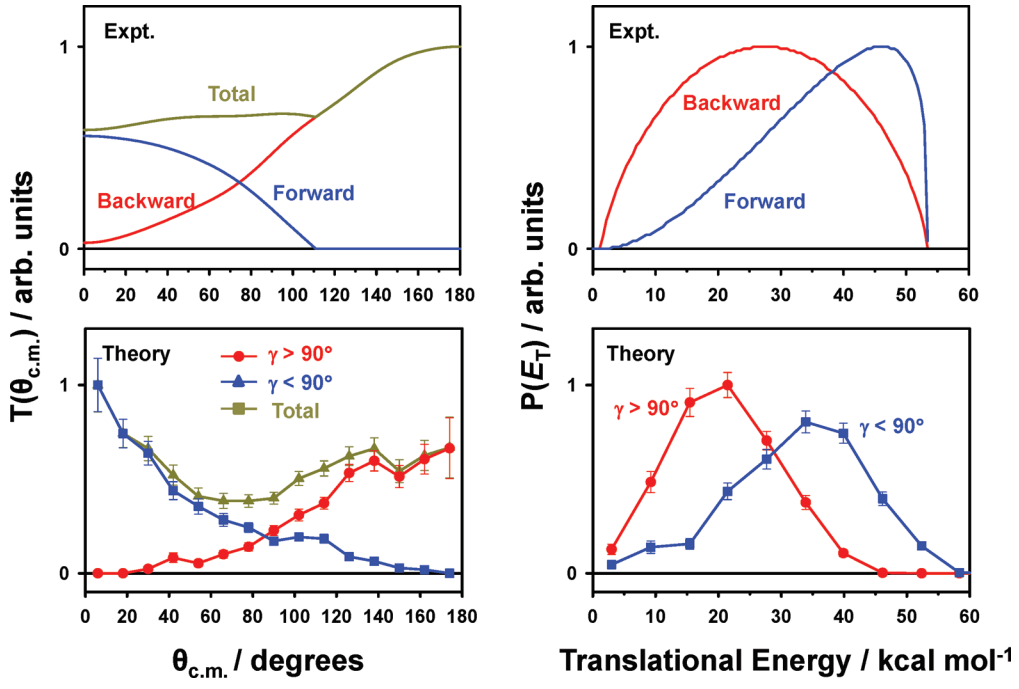

Figure 9. Center-of-mass angular and translational energy distributions for reactive scattering of ClO following reaction of $O(^3P)$ with DCl at $\langle E_{coll} \rangle = 92.2$ kcal mol^{-1}, derived from experiment (top panels) and from direct dynamics calculations at the B3LYP/6-31G(d,p) level of theory (bottom panels).

also been observed for hyperthermal interactions of O + CO[54] and Ar + C_2H_6.[55]

B. Reactive Scattering. $O(^3P)$ + HCl → OH + Cl. The dynamics of reactive scattering to produce OH + Cl are similar to those of inelastic scattering. The OH is strongly forward scattered in the c.m. reference frame with respect to the initial direction of the reagent O atom, and the translational energy distribution peaks at near available energy. Both these phenomena suggest a stripping mechanism involving collisions with large impact parameters. Calculations[1] show that the geometry of the transition state to form OH is bent, with an O−H−Cl angle of 135.9°. Therefore, at collision energies only slightly higher than the reaction barrier, OH would be expected to form through collisions with small impact parameters, which would lead to backward and sideways scattering of the OH. However, when the collision energy is increased to hyperthermal energies, which are tens of kcal mol^{-1} above the barrier, the geometrical constraints on the reaction are relaxed. Thus, OH may still be formed through large-impact-parameter collisions, resulting in predominantly forward scattering of OH. Similar behavior was

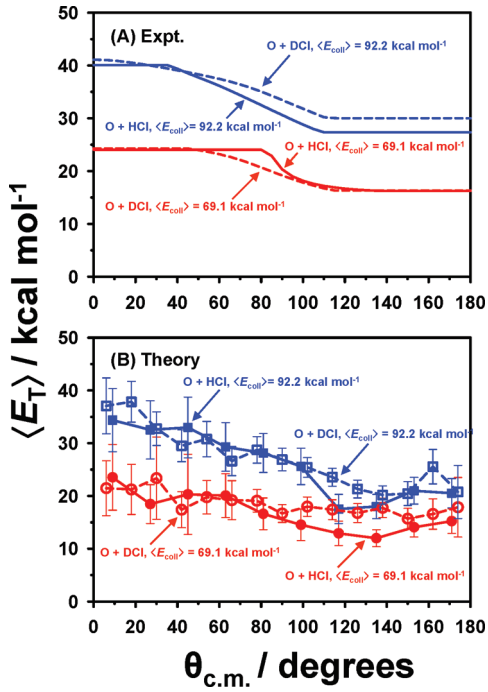

Figure 10. Average translational energy release as a function of c.m. angle for reactive scattering of ClO, from experimental measurements and direct dynamics calculations at the B3LYP/6-31G(d,p) level of theory with $\langle E_{coll} \rangle$ = 69.1 and 92.2 kcal mol^{-1}.

observed in the H-atom abstraction channels for hyperthermal reactions of O + CH_4[56] and O + C_2H_6.[57]

Compared to the inelastic scattering dynamics of O, both the c.m. angular distribution and the translational energy distribution of scattered OH are broader. On average, about 82% and 85% of the available energy are partitioned into translation at collision energies of 69.1 and 92.2 kcal mol^{-1}, respectively. In other words, about 11.6 and 13.1 kcal mol^{-1} of energy on average is converted into internal energy of OH. The low energy tail of the translational energy distribution indicates that more than 30 kcal mol^{-1} of energy can be converted into internal energy of OH, which might lead to vibrationally excited OH in the v′ = 2 level. In the current experiment, we cannot measure directly how the energy is partitioned into vibration and rotation; however, the partitioning of internal energy has been addressed in quantum mechanical and quasi-classical trajectory calculations by Xie et al.[24] They found that at a collision energy of 85 kcal mol^{-1}, the vibrational partitioning of OH(v′ = 0):OH(v′ = 1):OH(v′ = 2) is about 57:35:8. The rotational distributions peak at j' = ~18 and ~14 and extend to j' = ~35 for OH(v′ = 0) and OH(v′ = 1), respectively. The high rotational excitation of OH is presumably the result of a loose transition state geometry that has a broad cone of acceptance, allowing O−H−Cl angles away from the 135.9° saddle point and scattering of OH into the forward direction.

C. Reactive Scattering. O(^{3}P) + HCl/DCl → ClO + H/D. The c.m. translational energy distributions for the ClO + H/D channel are relatively broad. On average, about 23−45% (depending on $\theta_{c.m.}$) of the available energy goes into translation. Most of the available energy is partitioned into internal energy of the ClO product, and ClO starts to dissociate at collision energies higher than 102 kcal mol^{-1}. Therefore, the excitation function of ClO increases from threshold, reaches a maximum, and then decreases when the fragmentation process starts to dominate at high collision energies. The ClO excitation function rises dramatically from threshold, which is probably due to the large target that the Cl atom provides once the ClO + H channel is energetically allowed and the increasing ability for the reaction to deviate from the minimum energy path at higher collision energies. The total cross section for ClO + H and Cl + O + H continues to rise, indicating that the reaction cross section corresponding to O-atom attack on the Cl side of HCl continues to increase over the range of collision energies studied.

The good agreement between the shapes of the experimental excitation function for ClO and the corresponding B3LYP theoretical excitation function (see Figure 12), which was calculated assuming reaction only on the lowest ^{3}A″ surface, suggests that the bulk of the dynamics are explained by the single-surface calculations. In earlier studies from our laboratories on the H-atom elimination reactions, O + H_2 → OH + H[47] and O + CH_4 → OCH_3 + H,[48] an excited ^{3}A′ contribution was required to explain the observed excitation function. Although the cone of acceptance for the higher energy surface is smaller,[29] the necessity of the inclusion of both surfaces for some H-atom elimination reactions while only the lower energy surface was sufficient to explain the observed data for the O + HCl → ClO + H reaction may lead one to speculate that the present result is the fortuitous outcome of the inaccuracies in the B3LYP calculations. This is an open question that we intend to explore with more accurate MRCI calculations on both surfaces.

The experimental excitation function locates the reaction barrier near 46 kcal mol^{-1}, which is in close agreement with the B3LYP result but significantly lower than the earlier CCSD(T)/cc-pVTZ calculation of Camden and Schatz.[29] Higher level ab initio calculations in one of our laboratories show improved agreement with the experimental result and are in preparation for publication.

The scattering dynamics of ClO change qualitatively with increasing collision energy. At a lower collision energy, for example, 69.1 kcal mol^{-1}, ClO is mainly backward scattered in the c.m. reference frame with respect to the initial direction of the reagent O atom. A relatively small fraction of the ClO molecules are scattered in the sideways and forward directions. As the collision energy increases, the fraction of forward-scattered ClO increases and becomes comparable to the backward-scattered fraction at a collision energy of 92.2 kcal mol^{-1}. At a collision energy of 138.4 kcal mol^{-1}, ClO molecules are predominantly scattered in the forward direction. The reactive events that scatter ClO into the forward and backward directions also have different translational energy distributions. As mentioned in the previous section, two sets of $P(E)$ and $T(\theta)$ distributions had to be used to fit the experimental data in the forward-convolution analysis, one for forward scattering and one for backward scattering. Theoretical calculations also show that the c.m. translational energy distributions are different for forward and backward scattering. It is clear that the forward and backward scattering of ClO originate from different dynamical processes.

The theoretical calculations provide insight about the reaction mechanism, and indeed, the trajectories that lead to forward and backward scattering of ClO have different collision geometries. The minimum energy path to produce ClO + H has a bent configuration with an O−Cl−H angle of 158.0° and is product-like. At lower collision energies above threshold and lower than 102 kcal mol^{-1}, the reaction pathways that follow the minimum energy path dominate. However, as indicated in Figure 12, the reaction pathways that are far from the minimum energy path (γ < 90°) are still appreciable even at a collision energy of 69 kcal mol^{-1}. The calculated trajectories that lead

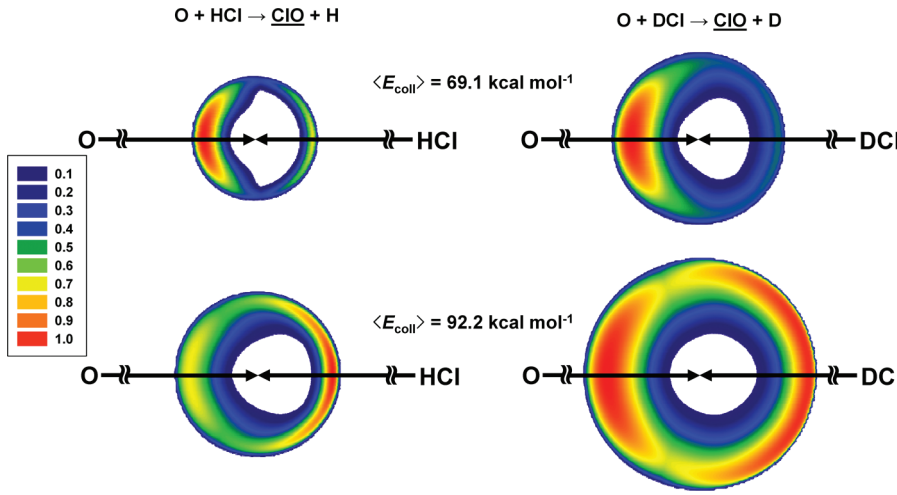

Figure 11. Experimental center-of-mass velocity-flux maps for reactive scattering of ClO following reaction of $O(^3P)$ with HCl or DCl at $\langle E_{coll} \rangle$ = 69.1 and 92.2 kcal mol^{-1}, derived from the angular and translational energy distributions shown in Figures 8, 9, SI-8, and SI-9. Each velocity-flux map is normalized such that the red color represents maximum flux.

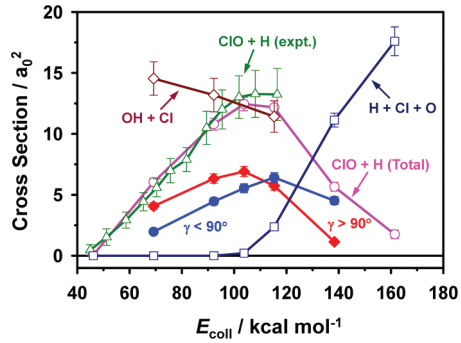

Figure 12. Experimental and theoretical excitation functions for the reaction of $O(^3P)$ with HCl. The blue and red curves show components of the theoretical ClO excitation function, distinguished by trajectories with $\gamma < 90°$ and $\gamma > 90°$, respectively.

to backward scattering of ClO are distinctly different than those that lead to forward-scattered ClO. When the O atom collides with the Cl atom of the HCl molecule at a large O−Cl−H angle ($\gamma > 90°$), the H atom is eliminated on the opposite side and the ClO is scattered backward. In this H + HL collision geometry, the H atom experiences a repulsive force from the Cl atom that is approximately independent of the nascent O−Cl bond, and the H atom is quickly ejected as the O atom approaches the Cl atom. Therefore, the H atom is eliminated with a translational energy that is determined by the repulsion from the Cl atom, so the energy that goes into translation of the product pair is largely independent of the collision energy. Because the maximum amount of translational energy of the product pair is limited,[29] more energy is partitioned into internal energy of ClO as the collision energy is increased, and secondary dissociation of the ClO will occur as soon as it is energetically allowed. The fraction of ClO products that dissociate thus increases with increasing collision energy above the threshold for secondary dissociation, and the cross section for producing ClO decreases. On the other hand, the trajectories that lead to forward scattering of ClO have collision geometries with small O−Cl−H angles ($\gamma < 90°$). The H atom in the HCl molecule is oriented toward the incoming O atom, and the O atom interacts with both the Cl atom and the H atom. Therefore, the H atom experiences a repulsive force from both the O and Cl atoms, and thus more energy may be released in translation with collision geometries with $\gamma < 90°$ than those with $\gamma > 90°$. Trajectories with $\gamma < 90°$ have lower cross sections for ClO production than those with $\gamma > 90°$ up to the threshold collision energy for secondary dissociation, but the relative cross sections of the two types of trajectory switch at higher collision energies (see Figure 12) because the trajectories with $\gamma < 90°$ tend to release more energy into translation and can lead to stable ClO products even when the available energy is more than sufficient to allow for secondary dissociation of ClO. The trajectories that produce stable ClO at high collision energies lead to forward scattering of ClO, so the angular distribution of ClO becomes predominantly forward at high collision energies.

The substitution of H with D alters the excitation function, and this isotope effect can be seen in the results of the QCT calculations that were run on the KSG surface (see Figure SI-11 (Supporting Information)). Despite the deficiencies of this surface, the calculations qualitatively capture the reaction dynamics. Because the D atom can carry away more energy in translation than the H atom, the ClO product of the O + DCl reaction is stable at collision energies higher than those for the ClO product of the O + HCl reaction, and the excitation function for the O + DCl reaction has a maximum at a higher collision energy.

The dynamics described above are believed to be general for H + HL systems at high collision energies. There is a close analogy in the H-atom elimination channel of the $O(^3P) + H_2O$ reaction.[32] In addition, earlier work on $O(^3P) + CH_4$[56] and $O(^3P) + C_2H_6$[57] show that H-atom elimination reactions occur with two distinct mechanisms, each of which has a saddle point. One has an O−C−H collinear configuration, and the other has a near perpendicular configuration with a slightly higher barrier. The angular distributions are quite broad but with more flux scattered into the backward hemisphere. The collisions with the collinear saddle point lead to backward scattering of the alkoxy products, and the collisions with the perpendicular saddle point lead to forward and sideways scattering. The energy is preferentially partitioned into internal energy and the fraction of internal energy increases with collision energy, a trend that is noticeably opposite to that of the H-atom abstraction channel. However, the calculations were not done at collision energies high enough to observe the fragmentation pathway.

Reaction mechanisms that do not follow the minimum energy path are not uncommon. Examples are the roaming mechanism in the photodissociation of formaldehyde to form $H_2 + CO$[58] and acetaldehyde to form $CH_4 + CO$,[59] an indirect mechanism

that violates the kinematic limit in H + HBr → H_2 + Br[60] and H + CD_4 → HD + CD_3,[61] and the chattering hydrogen atom mechanism in Cl + C_2H_6 → HCl + C_2H_5.[62] These mechanisms lead to greater internal excitation in the products. As discussed above, the dominant mechanism for O + HCl → ClO + H at high collision energies does not correspond to motion near the minimum energy path. This should be a general feature of light atom eliminations in hyperthermal reactions of the H + HL configuration. Reaction mechanisms that bypass the transition state or do not involve a transition state are possible and indeed may be ubiquitous.

VI. Concluding Remarks

The hyperthermal reaction of O(^{3}P) with HCl and DCl was investigated with crossed molecular beams methods at c.m. collision energies from 45 to 116 kcal mol^{-1}. The experimental findings were augmented by direct dynamic calculations at c.m. collision energies from 45 to 161 kcal mol^{-1}. The reaction may proceed through two primary pathways, H-atom abstraction to produce OH/OD + Cl and H-atom elimination to produce ClO + H/D, and the relative yields of these reactions become comparable at hyperthermal collision energies. The H-atom abstraction reaction proceeds through a stripping mechanism with large impact parameters, and the OH products predominantly scatter in the forward direction with little change in direction and energy with respect to the reagent O atom. The dynamics of H-atom abstraction are similar to those of inelastic scattering. The H-atom elimination reaction requires collisions with small impact parameters. The dynamics of ClO scattering strongly depend on collision energy. The shape of the experimental excitation function matched the excitation function calculated at the B3LYP/6-31G(d,p) level of theory. Direct dynamics calculations showed that the excitation function for production of ClO rises from threshold to a maximum near 115 kcal mol^{-1} and then decreases when ClO can be formed with sufficient internal energy to dissociate. At collision energies up to ∼115 kcal mol^{-1}, the dominant reactive trajectories are those in which the H atom is oriented away from the reagent O atom as it collides with the HCl molecule. These trajectories lead mainly to backward scattering of the ClO product with respect to the initial direction of the reagent O atom. The H-atom elimination reaction may also follow trajectories in which the H atom is oriented toward the reagent O atom as it collides with the HCl molecule. These trajectories lead mainly to forward scattering of the ClO product, and they channel more energy into translation of the product pair. Such trajectories do not represent motion along the minimum energy path. When the collision energy is high enough to allow for secondary dissociation of ClO (greater than ∼115 kcal mol^{-1}), ClO is produced predominantly by trajectories of the latter type, because they channel more energy into translation and lead to stable ClO. At collision energies above ∼130 kcal mol^{-1}, the process with the highest cross section is one that resembles the ClO + H channel (reaction 2) but which yields Cl + O + H rather than the primary products. The observed collision-energy-dependent scattering dynamics may pertain generally to H-atom elimination reactions in heavy + heavy-light reactions at hyperthermal collision energies.

Acknowledgment. This work was supported by grants from the Air Force Office of Scientific Research (FA9550-04-1-0428 and FA9550-07-1-0095) and by the Missile Defense Agency under Cooperative Agreement HQ0006-05-2-0001. A.L.B. is grateful for fellowships from the Zonta Foundation and the Montana Space Grant Consortium.

Supporting Information Available: Figures showing an enthalpy diagram, collision energy distributions, Newton diagrams, excitation functions, TOF distributions, and center-of-mass angular and translational energy distributions. This material is available free of charge via the Internet at http://pubs.acs.org.

References and Notes

(1) Ramachandran, B.; Peterson, K. A. *J. Chem. Phys.* **2003**, *119*, 9590.
(2) Ravishankara, A. R.; Smith, G.; Watson, R. T.; Davis, D. D. *J. Phys. Chem.* **1977**, *81*, 2220.
(3) Johnston, H. S. *Annu. Rev. Phys. Chem.* **1992**, *43*, 1.
(4) Smith, I. W. M. Bimolecular Collisions. In *Advances in Gas-Phase Photochemistry and Kinetics*; Ashfold, M. N. R., Baggott, J. E., Eds.; Royal Society of Chemistry: Letchworth, 1989; p 53.
(5) Zhang, R.; van der Zande, W. J.; Bronikowski, M. J.; Zare, R. N. *J. Chem. Phys.* **1990**, *94*, 2704.
(6) Koizumi, H.; Schatz, G. C.; Gordon, M. S. *J. Chem. Phys.* **1991**, *95*, 6421.
(7) Ramachandran, B.; Senekowitsch, J.; Wyatt, R. E. *J. Mol. Struct.* **1996**, *388*, 57.
(8) Ramachandran, B.; Schrader, E. A., III; Senekowitsch, J.; Wyatt, R. E. *J. Chem. Phys.* **1999**, *111*, 3862.
(9) Hsiao, C. C.; Lee, T. P.; Wang, N. S.; Wang, J. H.; Lin, M. C. *J. Phys. Chem. A* **2002**, *106*, 10231.
(10) Rakestraw, D. J.; McKendrick, K. G.; Zare, R. N. *J. Chem. Phys.* **1987**, *87*, 7341.
(11) Sato, S. *J. Chem. Phys.* **1955**, *23*, 592.
(12) Sato, S. *J. Chem. Phys.* **1955**, *23*, 2465.
(13) Kuntz, P. J.; Nemeth, E. M.; Polanyi, J. C.; Rosner, S. D.; Young, C. E. *J. Chem. Phys.* **1966**, *44*, 1168.
(14) Persky, A.; Broida, M. *J. Chem. Phys.* **1984**, *81*, 4352.
(15) Gordon, M. S.; Baldridge, K. K.; Bernholdt, D. E.; Bartlett, R. J. *Chem. Phys. Lett.* **1989**, *158*, 189.
(16) Moribayashi, K.; Nakamura, H. *J. Phys. Chem.* **1995**, *99*, 15410.
(17) Thompson, W. H.; Miller, W. H. *J. Chem. Phys.* **1997**, *106*, 142.
(18) Nobusada, K.; Moribayashi, K.; Nakamura, H. *J. Chem. Soc., Faraday Tran.* **1997**, *93*, 721.
(19) Ramachandran, B.; Senekowitsch, J.; Wyatt, R. E. *Chem. Phys. Lett.* **1997**, *270*, 387.
(20) Skokov, S.; Zou, S.; Bowman, J. M.; Allison, T. C.; Truhlar, D. G.; Lin, Y.; Ramachandran, B.; Garrett, B. C.; Lynch, B. J. *J. Phys. Chem. A* **2001**, *105*, 2298.
(21) Nobusada, K.; Nakamura, H.; Lin, Y.; Ramachandran, B. *J. Chem. Phys.* **2000**, *113*, 1018.
(22) Skokov, S.; Tsuchida, T.; Nanbu, S.; Bowman, J. M.; Gray, S. K. *J. Chem. Phys.* **2000**, *113*, 227.
(23) Xie, T.; Bowman, J. M.; Peterson, K. A.; Ramachandran, B. *J. Chem. Phys.* **2003**, *119*, 9601.
(24) Xie, T.; Bowman, J. M.; Duff, J. W.; Braunstein, M.; Ramachandran, B. *J. Chem. Phys.* **2005**, *122*, 014301.
(25) Gimelshein, S. F.; Levin, D. A.; Alexeenko, A. A. *J. Spacecr. Rockets* **2004**, *41*, 582.
(26) Minton, T. K.; Garton, D. J. Dynamics of Atomic-Oxygen-Induced Polymer Degradation in Low Earth Orbit. In *Advanced Series in Physical Chemistry: Chemical Dynamics in Extreme Environments*; Dressler, R., Ed.; World Scientific: Singapore, 2000.
(27) Murad, E. *J. Spacecr. Rockets* **1996**, *33*, 131.
(28) Troya, D.; Schatz, G. C. *Int. Rev. Phys. Chem.* **2004**, *23*, 341.
(29) Camden, J. P.; Schatz, G. C. *J. Phys. Chem. A* **2006**, *110*, 13681.
(30) Zhang, J.; Camden, J. P.; Brunsvold, A. L.; Upadhyaya, H. P.; Minton, T. K.; Schatz, G. C. *J. Am. Chem. Soc.* **2008**, *130*, 8896.
(31) Camden, J. P.; Dawes, R.; Thompson, D. L. *J. Phys. Chem. A* **2009**, *113*, 4626.
(32) Brunsvold, A. L.; Zhang, J.; Upadhyaya, H. P.; Minton, T. K.; Camden, J. P.; Paci, J. T.; Schatz, G. C. *J. Phys. Chem. A* **2007**, *111*, 10907.
(33) Press, W. H.; Flannery, B. P.; Teukolsky, S. A.; Vetterling, W. T. *Numerical Recipes in FORTRAN: The Art of Scientific Computing*, 2nd ed.; Cambridge University Press: Cambridge, England, 1992.
(34) Bunker, D. L. In *Proceedings of the International School of Physics Enrico Fermi Course XLIV: Molecular Beam and Reaction Kinetics*; Schlier, C., Ed.; Academic Press: New York, 1970; p 315.
(35) Kumar, S.; Sathyamurthy, N.; Ramaswamy, R. *J. Chem. Phys.* **1995**, *103*, 6021.
(36) Troya, D.; Lakin, M. J.; Schatz, G. C.; González, M. *J. Chem. Phys.* **2001**, *115*, 1828.
(37) Dong, E.; Setser, D. W.; Hase, W. L.; Song, K. *J. Phys. Chem. A* **2006**, *110*, 1484.
(38) Zhang, J.; Garton, D. J.; Minton, T. K. *J. Chem. Phys.* **2002**, *117*, 6239.
(39) Lee, Y. T.; McDonald, J. D.; LeBreton, P. R.; Herschbach, D. R. *Rev. Sci. Instrum.* **1969**, *40*, 1402.

(40) O'Laughlin, M. J.; Reid, B. P.; Sparks, R. K. *J. Chem. Phys.* **1985**, *83*, 5647.
(41) Garton, D. J.; Brunsvold, A. L.; Minton, T. K.; Troya, D.; Maiti, B.; Schatz, G. C. *J. Phys. Chem. A* **2006**, *110*, 1327.
(42) Lee, Y. T. Reactive Scattering I: Nonoptical Methods. In *Atomic and Molecular Beam Methods*; Scoles, G., Ed.; Oxford University Press: New York, 1988; Vol. 1; p 553.
(43) Buss, R. J. Crossed Molecular Beam Studies of Unimolecular Reaction Dynamics. Ph.D. thesis, University of California, Berkeley, 1979.
(44) Zhao, X. Photodissociation of Cyclic Compounds in a Molecular Beam. Ph.D. thesis, University of California, Berleley, 1988.
(45) Auerbach, D. J. In *Atomic and Moleular Beam Methods*; Scoles, G., Ed.; Oxford University Press: New York, 1988; Vol. 1; pp 362.
(46) Caledonia, G. E.; Krech, R. H.; Green, D. B. *AIAA J.* **1987**, *25*, 59.
(47) Garton, D. J.; Minton, T. K.; Maiti, B.; Troya, D.; Schatz, G. C. *J. Chem. Phys.* **2003**, *118*, 1585.
(48) Troya, D.; Schatz, G. C.; Garton, D. J.; Brunsvold, A. L.; Minton, T. K. *J. Chem. Phys.* **2004**, *120*, 731.
(49) Riahi, R.; Teulet, P.; Lakhdar, Z. B.; Gleizes, A. *Eur. Phys. J. D* **2006**, *40*, 223.
(50) Joshipura, K. N.; Vinodkumar, M.; Patel, U. M. *J. Phys. B* **2001**, *34*, 509.
(51) Antony, B. K.; Joshipura, K. N.; Mason, N. J. *Int. J. Mass Spectrom.* **2004**, *233*, 207.
(52) Baluja, K. L.; Mason, N. J.; Morgan, L. A.; Tennyson, J. *J. Phys. B* **2000**, *33*, L677.
(53) Balucani, N.; Beneventi, L.; Casavecchia, P.; Volpi, G. G. *Chem. Phys. Lett.* **1991**, *180*, 34.
(54) Brunsvold, A. L.; Upadhyaya, H. P.; Zhang, J.; Cooper, R.; Minton, T. K.; Braunstein, M.; Duff, J. W. *J. Phys. Chem. A* **2008**, *112*, 2192.
(55) Brunsvold, A. L.; Garton, D. J.; Minton, T. K.; Troya, D.; Schatz, G. C. *J. Chem. Phys.* **2004**, *121*, 11702.
(56) Troya, D.; Pascual, R. Z.; Schatz, G. C. *J. Phys. Chem. A* **2003**, *107*, 10497.
(57) Troya, D.; Pascual, R. Z.; Garton, D. J.; Minton, T. K.; Schatz, G. C. *J. Phys. Chem. A* **2003**, *107*, 7161.
(58) Townsend, D.; Lahankar, S. A.; Lee, S. K.; Chambreau, S. D.; Suits, A. G.; Zhang, X.; J., R.; Harding, L. B.; Bowman, J. M. *Science* **2004**, *306*, 1158.
(59) Houston, P. L.; Kable, S. H. *Proc. Natl. Acad. Sci. U.S.A.* **2006**, *103*, 16079.
(60) Pomerantz, A. E.; Camden, J. P.; Chiou, A. S.; Ausfelder, F.; Chawla, N.; Hase, W. L.; Zare, R. N. *J. Am. Chem. Soc.* **2005**, *127*, 16368.
(61) Camden, J. P.; Hu, W.; Bechtel, H. A.; Brown, D. J. A.; Martin, M. R.; Zare, R. N.; Lendvay, G.; Troya, D.; Schatz, G. C. *J. Phys. Chem. A* **2006**, *110*, 677.
(62) Huang, C.; Li, W.; Suits, A. G. *J. Chem. Phys.* **2006**, *125*, 133107.

JP101023Y